Experimental and Modeling Analysis of Diffusive Release from Single-Shell Microcapsules

Enrique Muñoz Tavera
Dept. of Mechanical Engineering and Materials Science, Rice University, Houston, TX 77251
Dept. of Physics and Astronomy, Rice University, Houston, TX 77251

Shyam B. Kadali and Hitesh G. Bagaria
Dept. of Chemical and Biomolecular Engineering, Rice University, Houston, TX 77251

Amy W. Liu
Dept. of Chemistry, Rice University, Houston, TX 77251

Michael S. Wong
Dept. of Chemical and Biomolecular Engineering, Rice University, Houston, TX 77251
Dept. of Chemistry, Rice University, Houston, TX 77251

DOI 10.1002/aic.11914

There is much experimental and mathematical work that describes chemical transport from multilayered films of planar geometries. There is less so, however, for chemical transport from multilayered spheres, a common structure for controlled-release materials. Based on the Sturm–Liouville approach of Ramkrishna and Amundson (1974), explicit analytical solutions for the concentration profiles and release kinetics from spherical capsules are presented. Fluorescent dye-release studies using single-shelled microspheres called nanoparticle-assembled capsules were performed to validate the model for uniformly and nonuniformly sized capsules. The combined experiment-modeling approach allows optical microscopy images and release measurements to be readily analyzed for estimating diffusion coefficients in capsule core and shell walls. © 2009 American Institute of Chemical Engineers *AIChE J,* 55: 2950–2965, 2009
Keywords: mass transfer, nanotechnology, mathematical modeling, controlled release formulations, composite materials

Introduction

The availability of new types of materials with engineered composition, porosity, internal gradation, and morphology is providing exciting opportunities in encapsulation and delivery applications, like in the biotechnology arena. Unilamellar and multilamellar vesicles, for example, have long been studied as drug and chemical delivery agents,[1,2] in which the

---

Additional Supporting Information may be found in the online version of this article.

Correspondence concerning this article should be addressed to M. S. Wong at mswong@rice.edu diffusive transport of molecules across the vesicle(s) membrane(s) is the common mode for drug release.[3–5] Other shell-like spherical structures, such as layer-by-layer-assembled capsules[6–8] and nanoparticle-assembled capsules,[9–12] are also possible encapsulation and delivery agents, with chemical release from these constructs demonstrated experimentally. The synthesis of spherical structures from the cross-linking of polyelectrolytes[13] to encapsulate whole cells,[14] enzymes and other proteins,[15–22] is a common practice to preserve biological or catalytic activity. In drug delivery applications,[23–27] spherical structures can be in the form of solid lipid particles,[28] chitosan nano and microspheres,[29–34] cross-linked polysaccharide microspheres,[35–37] and alginate microspheres.[18,21,38,39] Block copolymers are particularly suitable for the construction of spherical shell micelles,[40–48] because their physical and chemical properties can be controlled by adjusting the size and ratio of the constituting blocks,[48–53] as well as by physical-chemical agents such as temperature[54,55] and pH.[56,57]

The characterization of the release kinetics[21,22,33,34,40,44,46,47,58–62] from delivery structures is of primary importance for therapeutic applications, and mathematical modeling provides insights into the transport properties of these spherical materials, as a necessary complement to the experimental data. Mathematical modeling for drug release started with the Higuchi equation for planar structures,[63] later extended to spherical geometries.[64] These equations, or variants of them, are still broadly applied to interpret experimental data in drug release kinetics.[22,65–68] In particular, the Higuchi model relies on oversimplifying assumptions, such as a constant concentration gradient to drive the Fickian diffusion process, as reflected in the square-root time dependence for the release kinetics in the planar geometry case.[63] This description, whose main advantage is to keep simplicity in the analytical equations, is approximately correct for initial/intermediate times, but not for the long time behavior. Indeed, most experimental studies[21,33,40,44,58,60–62,68] show an asymptotic plateau in the fraction of substance released for sufficiently long times. This feature may be attributed to the continuous decrease in the concentration gradient between the delivery structure and the surrounding medium due to the gradual depletion of the capsule.

There exist more detailed mathematical models which successfully describe this effect,[67,69–76] including numerical simulation studies,[77–79] which typically consider uniform spherical spheres, described by a constant or a time-dependent effective diffusion coefficient. The majority of these models require numerical integration, with a few exceptions expressed in terms of closed analytical solutions ([72,73,67]). None of these analytical models can be applied to spheres with one or more shells.

Significant effort has been invested to describe in more detail the drug release process in polymeric structures, by considering a mechanism with different steps,[75,80–83] and Monte Carlo simulations[84,85] to take into account the polymer matrix degradation. Perhaps the complexity of these approaches has limited their practical use, as compared to simpler analytical models like the Higuchi equation.

For microcapsules with one and more layers (or shells), a mathematical description that considers different effective diffusion coefficients for each layer is more appropriate than assuming uniform materials properties. This approach has been previously implemented and solved numerically for skin in a planar geometry.[86,87] To our knowledge, however, no analytical solutions have been presented for the release kinetics in multilayered spherical geometries.

In this article, we present the analytical solution for a mathematical model that describes unsteady-state transport from multilayered spheres. Our analysis builds on the formalism of Ramkrishna and Amundson,[88] which was originally proposed for one-dimensional problems. In this form, it has been applied to model electrophoretic transport,[89–91] microwave heating[91] and reaction-diffusion[91] in one-dimensional geometries. The method is based on the finite Fourier-transform expansion of eigenfunctions of self-adjoint, second-order Sturm–Liouville operators with discontinuous coefficients. This differs from other approaches based on Laplace transforms[92] or semianalytical methods.[93] The formalism of Ramkrishna and Amundson has been generalized to include curvature effects,[94,95] and applied in the context of heat conduction through multilayered cylinders and spheres,[96] and diffusion in cylindrical membranes.[97] To validate our analytical model with experimental dye-release results, we used nanoparticle-assembled microcapsules (NACs), a composite material comprised of a single layer (a polymer/nanoparticle shell with macroscopically uniform properties) surrounding a polymer/water interior, recently created in our laboratory.[9–11]

Experiments

Materials

Polyallylamine hydrochloride (PAH, 70,000 g/mol, ~750 allylamine units per molecule), fluorescein sodium salt, premixed phosphate buffered saline (PBS) salt mixture and glycine were purchased from Sigma-Aldrich. The premixed PBS salt was dissolved in deionized (DI) water to prepare the PBS buffer solution (pH = 7.4, ionic strength I = 165 mM). Glycine and NaOH buffers were prepared for a wide range of pH values (8.5 through 10.3) by mixing 0.2 M glycine and 0.2 M NaOH solutions made with DI water. Trisodium citrate dihydrate salt (citrate), NaOH pellets and 1 N HCl solution were obtained from Fisher Scientific. An aqueous colloidal suspension of silica NPs (Snowtex-O, 20.5 wt % silica, pH 3.5, ionic strength I = 16.9 mM)) was kindly provided by Nissan Chemicals. These NPs have a diameter of 13 ± 3 nm based on dynamic light scattering and a zeta potential value of −16 mV (Henry's equation) by electrophorectic measurements.[11] Deionized water from a Barnstead Nanopure Diamond System (18.2 MΩ) was used to prepare all the solutions.

Synthesis of dye-encapsulated NACs

NACs were synthesized by first mixing 14 ml of 5 mg/ml of PAH solution with 35 ml of 14.2 mM citrate solution in a 250 ml beaker under gentle magnetic stirring (speed "4" of 0 through 10) for 10 s. The resulting suspension turned turbid instantly indicating the formation of polymer-salt aggregates. After aging these aggregates for 20 min, 35 ml of a 1 mg/ml fluorescein sodium salt ("Na-Flu") dye solution was added under gentle magnetic stirring for 10 s. This mixture was aged for another 10 min and 35 ml of 1.2 wt %

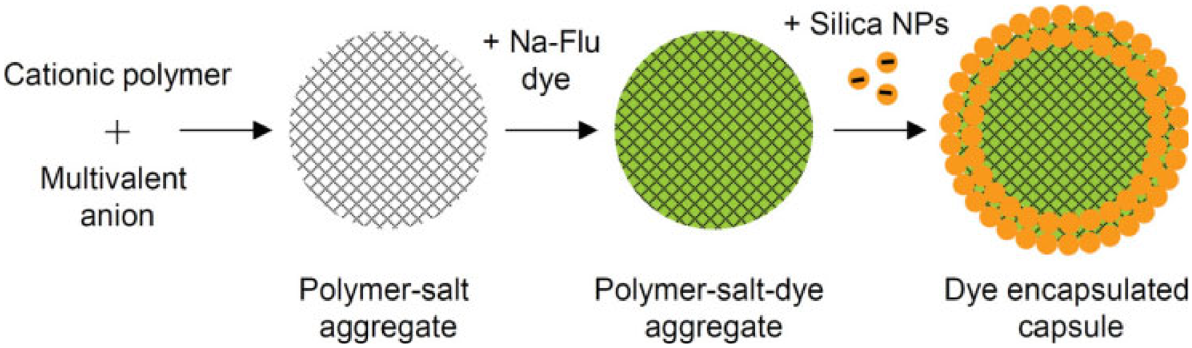

Figure 1. Schematic showing the synthesis of fluorescein-encapsulated NACs, with the shell made of NPs and polymer.

[Color figure can be viewed in the online issue, which is available at www.interscience.wiley.com.]

silica NP suspension (prepared by diluting with DI water and adjusting the pH to 3.5 with 1 N HCl solution) was added. The resulting mixture was stirred vigorously (speed "7") for 10 min and aged for 2 h to form Na-Flu-encapsulated NACs. A schematic of this mixing synthesis process is shown in Figure 1.

Dye release study

Before performing the dye release experiments, NACs were cleaned to remove the excess Na-Flu. The cleaning was performed by dispersing the NACs (by sonication for 30 s and stirring), and separating them by centrifugation (Beckman-Coulter Allegra X-22 centrifuge at 6000 rpm for 7 min). All the supernatant was carefully removed and capsules re-dispersed in 30 ml of PBS buffer solution. Another round of centrifugation was performed to ensure complete removal of any superficial Na-Flu. The supernatant was carefully decanted and NACs were redispersed in 30 ml of PBS to begin the dye release studies. The NACs solution was quickly pipetted into 1.5 ml aliquots and placed on a rocking platform to ensure that the capsules do not settle. At various intervals the aliquots were centrifuged for 5 min and UV–vis was performed on the supernatant to quantify the dye released (Supporting Information Fig S1). The amount of Na-Flu remaining in the capsules was also determined by breaking NACs with 1 N NaOH solution and performing UV–vis for mass balance verification. The mass balance of dye was found to be within 93% for all samples. The total amount of dye (capsule and supernatant) was found to be 1.5 μg in each aliquot. It should be noted that we assume dye release does not stop during the centrifugation, for which is accounted.

Characterization techniques

UV–vis Spectroscopy. A Shimadzu 2401-PC UV–vis spectrophotometer and standard poly(methyl methacrylate) cuvettes with a path length of 1 cm were used.

Optical and Fluorescence Microscopy. Optical and fluorescence microscopy images were collected with a Leica DM2500 upright microscope equipped with 100× oil immersion objective (Numerical Aperature 1.4). Fluorescence images of NACs were collected through a FITC filter box.

Confocal Microscopy. A Zeiss LSM 510 laser scanning confocal microscope utilizing a 63X Plan-Apochromat, (Numerical Aperture 1.4) was used to collect fluorescence image slices of the capsules.

Scanning Electron Microscopy. Scanning electron microscopy (SEM) was carried out using FEI Quanta 400 field emission scanning electron microscope. Secondary electron images of NACs were taken at 20 kV electron beam with a working distance of 10 mm. The NACs suspension containing dye were washed twice with water, loaded on an aluminum stub and dried. The sample was sputter-coated with gold for 1 min ($\sim$25 nm of Au film) prior to imaging.

Coulter Counter. Capsule diameter distribution and the volume fraction of the capsules in the suspension was measured with a Beckman Coulter counter having an orifice diameter of 100 μm. The lower limit for measuring sizes for this orifice was 2 μm. The instrument calibration was verified by measuring 10 μm standard latex beads. The diameter of capsules was measured by diluting $\sim$10 μl of the NACs PBS suspension in 20 ml of aqueous Isotone solution (composition: 7.93 g/l NaCl, 0.38 g/l Na_2EDTA, 0.40 g/l KCl, 0.19 g/l H_2NaPO_4, 1.95 g/l HNa_2PO_4, 0.30 g/l NaF; Beckman Coulter).

Quartz Crystal Microbalance with Dissipation Monitoring. A quartz crystal microbalance with dissipation monitoring (QCM-D; Q-sense E4) was used in this study. Gold-coated quartz crystal sensors were used (also from Q-sense). The resonance frequency of the crystal sensor was 4.95 MHz ± 50 kHz and was excited during experimentation at the fundamental frequency, as well as the 3rd, 5th, 7th, 9th, 11th, and 13th overtones (15, 25, 35, 45, 55, and 65 MHz, respectively). The Sauerbrey equation relates change in frequency of the oscillating sensor to the change in adsorbed mass on the sensor by the following equation: $\Delta m = -C\bullet\Delta f/v$ where Δm is the change in mass, or mass of the deposited film; C is a constant (= 17.7 ng cm^2 Hz^{-1} at $f_{n=1} = 5$ MHz), Δf is the change in frequency of the oscillating system, and v is the overtone number. Solutions of aqueous PAH and Na_3Cit were vortexed together for 10 s and aged for 10 min. This suspension was then flowed through the Q-sense E4 chamber with the mounted sensor for about 25 h. Milli-Q water was then passed through the chamber to rinse off any excess polymer-salt from the surface of the sensor for $\sim$30 min, which was then followed by an aqueous solution of Na-Flu through the chamber for 8 h.

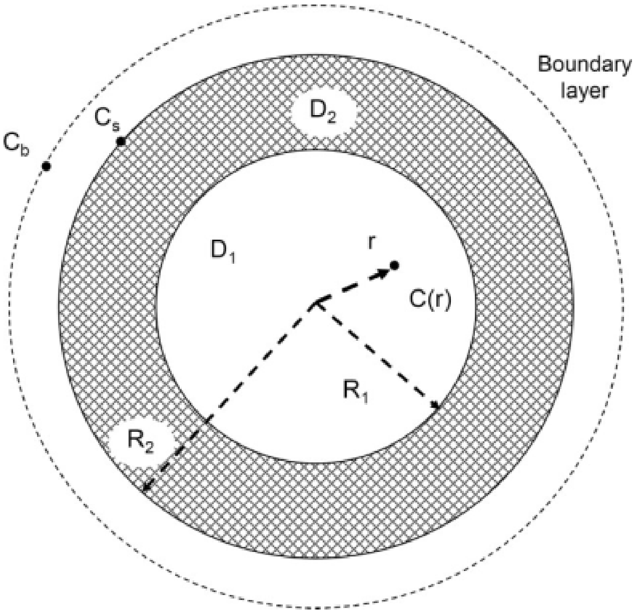

Figure 2. Geometry of single-shell capsule.

Different diffusion coefficients D_1, D_2 are considered for the core region ($r < R_1$) and shell region ($R_1 < r < R_2$). The concentration at the external surface, C_s, is differentiated from the bulk concentration, C_b, due to the presence of an external boundary layer.

Results and Discussion

NACs were chosen over other capsular types because their structure is robust enough to be handled under wet and dry conditions; their composite shell wall has previously been shown to have semipermeability characteristics; and shell properties can be controlled readily at the synthesis level.[9–11] This nanostructured material has a thick (hundreds of nanometer), semipermeable shell composed of NPs held together by the oppositely charged PAH polymer, and a core that contains the polymer-salt aggregate. The structure is thus modeled as a single-layer sphere with inner and outer radii $R_1 < R_2$ (Figure 2), which we assume to be unchanged over time. This assumption neglects volume changes due to polymer matrix degradation[84] or swelling effects in the capsule interior. Different diffusion coefficients of a given molecular compound will be considered, D_1 for the core region (polymer/salt matrix) and D_2 for the shell region (polymer/NP composite). We will assume that the external liquid medium is well mixed, and acts as a perfect sink with a bulk concentration C_b. In general, due to the external mass transfer resistance imposed by the boundary layer which surrounds the capsular structure, the bulk concentration may differ from the external surface concentration C_s.

In polymeric structured microcapsules, the solubility of the drug may differ in regions with different polymer concentrations,[98,99] thus affecting the encapsulation efficiency and the release rate. This effect can be described by a partition coefficient to relate the concentrations of the encapsulated drug at both sides of an interface. Partition coefficients are also important for drug encapsulation in lipid vesicles[100] and other micro-emulsions,[101] and in polymer-lipid microcapsules,[78] all of them possessing approximately spherical geometries. In our model, we will assume a partition coefficient P_{12} to define the ratio between the concentrations of the encapsulated substance at both sides of the interface at $r = R_1$, and a partition coefficient P_{2b} between the shell region and the bulk fluid.

Based on this simplified picture, we will present analytical solutions for a model of diffusive release from solute-containing NACs by considering two different types of boundary conditions.

As depicted in Figure 2, the diffusion coefficients for the drug in the core and shell materials are different, and assumed to have constant effective values D_1 and D_2, respectively. This situation can be mathematically stated as

$$D(r) = \begin{cases} D_1 & 0 \le r < R_1 \\ D_2 & R_1 < r \le R_2 \end{cases} \tag{1}$$

We look for the concentration profile $C(r,t)$ inside the microcapsule, from the solution of the partial differential equation

$$\frac{1}{r^2}\frac{\partial}{\partial r}\left(r^2 D(r)\frac{\partial C}{\partial r}\right) = \frac{\partial C}{\partial t} \tag{2}$$

We assume that initially, the substance is distributed between core and shell with a ratio $\sigma > 1$. This is represented by the initial condition

$$C(r, t = 0) = \begin{cases} C_0 & 0 \le r < R_1 \\ \sigma C_0 & R_1 < r < R_2 \end{cases} \tag{3}$$

The continuity conditions at the interface $r = R_1$ are given by

$$\begin{gathered} C\left(r = R_1^-\right) = P_{12} C\left(r = R_1^+\right) \\ D_1 \frac{\partial C}{\partial r}\left(r = R_1^-\right) = D_2 \frac{\partial C}{\partial r}\left(r = R_1^+\right) \end{gathered} \tag{4}$$

Here, P_{12} represents a partition coefficient for the diffusing solute between the core and shell materials.

As the origin $r = 0$ is included in the domain of the problem, it is necessary to consider the additional condition

$$\lim_{r \to 0} C(r, t) = \text{finite} \tag{5}$$

For the external boundary condition, we consider that release from the drug-containing microcapsule structure occurs within a flow field. Therefore, the overall mass transfer must account for convection through the boundary layer. The relative importance of diffusion over convection is given by the Pèclet number,[102] $Pe = Re\ Sc$. The Reynolds and Schmidt numbers are defined by $Re = V(2R_2)/\mu\rho$ and $Sc = \mu/\rho D_f$, respectively, where V, μ, and ρ are the fluid velocity, viscosity, and density, and D_f is the solute diffusion coefficient in the fluid. At relatively small Pe values, interfacial mass transfer can be considered to occur through a thin boundary layer,[102] and modeled by a mass transfer coefficient k_c. Assuming a partition coefficient P_{2b} between the shell and the bulk fluid, the appropriate boundary condition for this situation is

$$-D_2 \frac{\partial C}{\partial r}(R_2, t) = k_c(P_{2\mathrm{b}} C(R_2, t) - C_\mathrm{b}) \tag{6}$$

Here, C_b is the external bulk concentration as depicted in Figure 2, which is assumed to be approximately constant over the experiment. This approximation is justified by the small volume fraction of capsules that was found to be $V_\mathrm{capsules}/V_\mathrm{suspension} = 0.18$ (ml)/30 (ml) = 0.006 based on Coulter counter measurements. As a result the concentration of the solute goes from 0 for the initial time point to a maximum of only 0.5 μg/ml (or 0.5 ppm) at steady state. (Supporting Information Table S1).

The steady-state solution of Eq. 2 corresponding to the boundary condition Eq. 6 is given by $C^\mathrm{ss}(r)$,

$$C^\mathrm{ss}(r) = \begin{cases} \frac{P_{12}}{P_{2\mathrm{b}}} C_\mathrm{b} & 0 \le r < R_1 \\ \frac{C_\mathrm{b}}{P_{2\mathrm{b}}} & R_1 < r \le R_2 \end{cases} \tag{7}$$

To solve the general unsteady-state problem, it is convenient to define the dimensionless concentration

$$\Phi(x, \tau) = (C(r, t) - C^\mathrm{ss}(r))/C_0, \tag{8}$$

with $C^\mathrm{ss}(r)$ defined by Eq. 7. The boundary condition Eq. 6 in dimensionless form becomes

$$\frac{\partial \Phi}{\partial x}(1, \tau) = -Bi\, P_{2\mathrm{b}} \Phi(1, \tau). \tag{9}$$

Here, $Bi = k_\mathrm{c} R_2 / D_2$ is a mass transfer Biot number based on the external radius of the microcapsule and the shell diffusion coefficient. The Biot number is directly proportional to the Sherwood number $Sh = k_\mathrm{c} R_2 / D_\mathrm{f} = Bi\, D_2 / D_\mathrm{f}$. Classical dimensional analysis[102] shows that $Sh \approx (Re\ Sc)^{1/3} \approx Pe^{1/3}$, indicating it is a measure of the mass transfer resistance imposed by the external boundary layer; the same argument applies for the Biot number. Eq. 9 technically corresponds to a Robin boundary condition[103]; dividing both sides by Bi and taking the limit $Bi \to \infty$ leads to a Dirichlet boundary condition $\Phi(1,\tau) = 0$. Thus, Eq. 9 describes a general situation of imperfect fluid mixing, and the limit $Bi \to \infty$ represents the ideal-mixing case.

As shown in detail in Appendix, we obtain the analytical solution

$$\begin{aligned} \Phi(x, \tau) = \sum_{k=1}^{\infty} B_1(\lambda_k) \Bigg[& \left(1 - \frac{P_{12}}{P_{2\mathrm{b}}} \frac{C_\mathrm{b}}{\mathrm{C}_0}\right) \left(\frac{\sin\left(x_1 \sqrt{\lambda_k}\right)}{\lambda_k} - \frac{x_1 \cos\left(x_1 \sqrt{\lambda_k}\right)}{\sqrt{\lambda_k}} \right) \\ & + \left(\sigma - \frac{1}{P_{2\mathrm{b}}} \frac{C_\mathrm{b}}{C_0}\right) P_{12} \alpha_k \left(\frac{1 - x_1 \cos\left((1 - x_1)\sqrt{\lambda_k/\gamma}\right)}{\sqrt{\lambda_k/\gamma}} - \frac{\sin\left((1 - x_1)\sqrt{\lambda_k/\gamma}\right)}{\lambda_k/\gamma} \right. \\ & \left. - \frac{\sqrt{\lambda_k/\gamma}}{1 - P_{2\mathrm{b}} Bi} \left(\frac{1 - \cos\left((1 - x_1)\sqrt{\lambda_k/\gamma}\right)}{\lambda_k/\gamma} + \frac{x_1 \sin\left((1 - x_1)\sqrt{\lambda_k/\gamma}\right)}{\sqrt{\lambda_k/\gamma)}} \right) \right) \Bigg] e^{-\lambda_k \tau} v_k(x) \end{aligned} \tag{10}$$

Here, the eigenvalues λ_k, $k = 1,2, \ldots ,\infty$ are obtained as the (infinitely many) solutions of the characteristic equation (Appendix)

$$\sin\left(x_1 \sqrt{\lambda}\right) = \frac{M_{12}(\lambda) M_{21}(\lambda)}{M_{22}(\lambda)} \tag{11}$$

with

$$\begin{aligned} M_{12}(\lambda) &= P_{12} \left[\frac{\sqrt{\lambda/\gamma}}{(1 - P_{2\mathrm{b}} Bi)} \cos\left((1 - x_1)\sqrt{\lambda/\gamma}\right) - \sin\left((1 - x_1)\sqrt{\lambda/\gamma}\right) \right] \\ M_{21}(\lambda) &= \sqrt{\lambda} x_1 \cos\left(x_1 \sqrt{\lambda}\right) - \sin\left(x_1 \sqrt{\lambda}\right) \\ M_{22}(\lambda) &= \gamma \left\{ \sqrt{\frac{\lambda}{\gamma}} x_1 \cos\left((1 - x_1)\sqrt{\lambda/\gamma}\right) + \sin\left((1 - x_1)\sqrt{\lambda/\gamma}\right) + \frac{\sqrt{\lambda/\gamma}}{1 - P_{2\mathrm{b}} Bi} \right. \\ & \quad \left. \times \left\{ \sqrt{\frac{\lambda}{\gamma}} x_1 \sin\left((1 - x_1)\sqrt{\lambda/\gamma}\right) - \cos\left((1 - x_1)\sqrt{\lambda/\gamma}\right) \right\} \right\} \end{aligned} \tag{12}$$

The eigenfunctions $v_k(x)$ in Eq. 10 are defined as (Appendix)

$$v_k(x) = B_1(\lambda_k) \times \begin{cases} \frac{\sin(x\sqrt{\lambda_k})}{x} & 0 \le x < x_1 \\ \alpha_k \left[\frac{\sin\left((1-x)\sqrt{\lambda_k/\gamma}\right)}{x} - \frac{\sqrt{\lambda_k/\gamma}}{1 - P_{2\mathrm{b}} Bi} \frac{\cos\left((1-x)\sqrt{\lambda_k/\gamma}\right)}{x} \right] & x_1 < x \le 1 \end{cases} \tag{13}$$

Here, the constants α_k are defined by (Appendix)

$$\alpha_k = \frac{\sin\left(x_1 \sqrt{\lambda_k}\right)}{P_{12} \left[\sin\left((1 - x_1)\sqrt{\lambda_k/\gamma}\right) - \frac{\sqrt{\lambda_k/\gamma}}{1 - P_{2\mathrm{b}} Bi} \cos\left((1 - x_1)\sqrt{\lambda_k/\gamma}\right) \right]} \tag{14}$$

and the coefficients $B_1(\lambda_k)$ are given by the equation (Appendix)

$$\begin{aligned} B_1(\lambda_k) = \Biggl[\frac{1}{2}\left(x_1 - \frac{\sin\left(2x_1\sqrt{\lambda_k}\right)}{2\sqrt{\lambda_k}}\right) \\ + \alpha_k^2 P_{12}\Biggl\{\frac{1}{2}\left(1 - x_1 - \frac{\sin\left(2x_1\sqrt{\lambda_k/\gamma}\right)}{2\sqrt{\lambda_k/\gamma}}\right) \\ + \frac{\cos\left(2\sqrt{\lambda_k/\gamma}(1-x_1)\right) - 1}{2(1-P_{2\mathrm{b}}Bi)} \\ + \frac{\lambda_k/\lambda}{(1-P_{2\mathrm{b}}Bi)^2}\frac{1}{2}\left(1 - x_1 + \frac{\sin\left(2x_1\sqrt{\lambda_k/\gamma}\right)}{2\sqrt{\lambda_k/\gamma}}\right)\Biggr\}\Biggr]^{-1/2} \end{aligned} \tag{15}$$

The concentration profile $C(r,t)$ is obtained from Eq. 8 in terms of $\Phi(r/R_2,tD_1/R_2^2)$, which is defined by Eq. 10

$$\frac{C(r,t)}{C_0} = \frac{C^{\mathrm{ss}}(r)}{C_0} + \Phi(r/R_2, tD_1/R_2^2) \tag{16}$$

Fractional release rate

One of the advantages of possessing an exact analytical solution for the concentration profile predicted by our model, is that it is relatively straightforward to derive analytical expressions for other variables of interest. In particular, for drug delivery applications, it is important to calculate the fractional release as a function of time, as defined by the ratio

$$\text{Fractional release} = \frac{M(t)}{M_\infty} \tag{17}$$

Here $M(t)$ is the total mass of the substance released up to time t, whereas M_∞ corresponds to the maximal amount of substance which can be released ($t \to \infty$).

An elementary mass-balance equation relates the rate of change in the amount of mass released from the microcapsule, with the mass flux at the surface, as follows

$$\begin{aligned} \frac{dM}{dt} &= -\iiint\limits_{V_{\text{capsule}}} \frac{\partial C}{\partial t} dV = -\iiint\limits_{V_{\text{capsule}}} \nabla\cdot(D\nabla C)dV \\ &= -\oiint\limits_{S_{\text{capsule}}} D\nabla C\cdot d\vec{S} = -4\pi R_2^2 D_2 \frac{\partial C}{\partial r}(R_2,t) \end{aligned} \tag{18}$$

The differential Equation (18) is integrated to obtain the total mass released up to time t, which is given by

$$M(t) = -4\pi R_2^2 D_2 \int_0^t \frac{\partial C}{\partial r}(R_2,t')dt' \tag{19}$$

Therefore, taking the appropriate ratio, a formula for the fractional release as defined in Eq. 17 is obtained

$$\frac{M(t)}{M_\infty} = \frac{\int_0^t \frac{\partial C}{\partial r}(r,t')dt'}{\int_0^\infty \frac{\partial C}{\partial r}(r,t')dt'} \tag{20}$$

By inserting the concentration profile defined by Eq. 16 into Eq. 20, we obtain an analytical expression for the fractional release

$$\frac{M(t)}{M_\infty} = 1 - \frac{\sum_{k=1}^{\infty} \frac{\alpha_k B_1(\lambda_k)}{\sqrt{\lambda_k}}\langle v_k,\Phi\rangle_0 e^{-\lambda_k \frac{D_1}{R_2^2}t}}{\sum_{k=1}^{\infty} \frac{\alpha_k B_1(\lambda_k)}{\sqrt{\lambda_k}}\langle v_k,\Phi\rangle_0} \tag{21}$$

Here, the coefficients α_k are defined by Eq. 14, the $B_1(\lambda_k)$ by Eq. 15, and the eigenvalues λ_k are obtained from Eqs. 11 and 12. The coefficients $\langle v_k, \Phi\rangle_0$ are defined by (Appendix)

$$\begin{aligned} &\langle v_k,\Phi\rangle_0 \\ &= B_1(\lambda_k)\Biggl[\left(1 - \frac{P_{12}}{P_{2\mathrm{b}}}\frac{C_\mathrm{b}}{\mathrm{C}_0}\right)\left(\frac{\sin\left(x_1\sqrt{\lambda_k}\right)}{\lambda_k} - \frac{x_1\cos\left(x_1\sqrt{\lambda_k}\right)}{\sqrt{\lambda_k}}\right) \\ &\quad + \left(\sigma - \frac{1}{P_{2\mathrm{b}}}\frac{C_\mathrm{b}}{\mathrm{C}_0}\right) \\ &+ P_{12}\alpha_k\Biggl(\frac{1 - x_1\cos\left((1-x_1)\sqrt{\lambda_k/\gamma}\right)}{\sqrt{\lambda_k/\gamma}} - \frac{\sin\left((1-x_1)\sqrt{\lambda_k/\gamma}\right)}{\lambda_k/\gamma} \\ &\quad - \frac{\sqrt{\lambda_k/\gamma}}{1-P_{2\mathrm{b}}Bi} \\ &\times\left(\frac{1-\cos\left((1-x_1)\sqrt{\lambda_k/\gamma}\right)}{\lambda_k/\gamma} + \frac{x_1\sin\left((1-x_1)\sqrt{\lambda_k/\gamma}\right)}{\sqrt{\lambda_k/\gamma}}\right)\Biggr)\Biggr] \end{aligned} \tag{22}$$

We notice that Eq. 21 corresponds to an (infinite) linear combination of exponential decays, a mathematical structure which is common in the solution of heat and mass transfer problems.[104–106] As the eigenvalues λ_k obtained after Eq. 13 are monotonically increasing positive numbers, the series converges for a finite number of terms. This feature can also be used to obtain simplified forms of Eq. 13 which can be applied as empirical models to fit experimental data, as discussed in Supporting Information.

From a numerical evaluation of Eq. 21, we noticed that under well mixed conditions ($Bi \gg 1$), the most relevant parameter controlling the steepness of the saturation curve is $\gamma = D_2/D_1$, the ratio between the shell and core effective diffusion coefficients. The reason for this is that an increase in the shell diffusion coefficient D_2 corresponds to a faster release of the encapsulated substance, and vice versa. Thus, this suggests that the release rate could be controlled by engineering the material properties of the shell that affect diffusion, for example, by tuning shell porosity using different sizes of the NPs that make up the shell.

Experimental analysis of dye-containing capsule structure

To compare our model predictions of the fractional release rate with experiments, the following parameters were required to be estimated from experiments: (i) x_1, the ratio between the inner and outer radii, (ii) P_{12}, partition coefficient between the polymer-salt aggregate and the interior of the shell, (iii) $P_{2\mathrm{b}}$, the partition coefficient between the outer shell surface

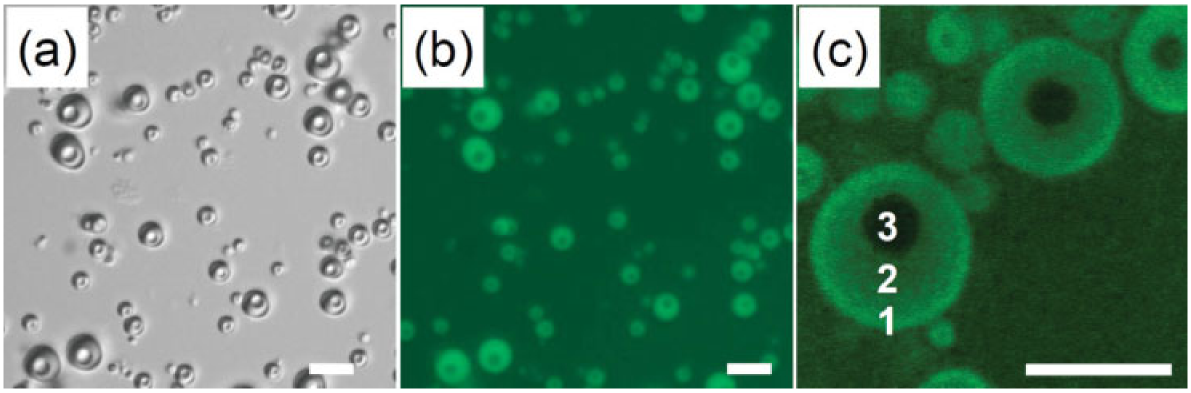

Figure 3. (a) Differential interference contrast optical image and (b) corresponding fluorescence image of Na—Flu encapsulated NACs. (c) Confocal microscopy image showing the three regions in Na—Flu encapsulated NACs. Scale bars: 10 μm.

[Color figure can be viewed in the online issue, which is available at www.interscience.wiley.com.]

and the bulk, (iv) σ, the ratio between the initial shell and core concentrations and (v) the mean capsule diameter and distribution. Optical DIC and fluorescence microscopy images of the Na–Flu encapsulated NACs were collected to estimate the first four parameters (Figures 3–5). The mean capsule diameter and distribution was determined by Coulter counter that was supported with SEM images (Figure 6).

The brightfield image in Figure 3a shows that the capsules had a thick shell wall and, occasionally, an off-center core, and the fluorescence image in Figure 3b suggests that the dye molecules were located throughout the capsule structure, with the negatively-charged dye associated with the positively-charged PAH polymer. With confocal microscopy providing cross-sectional imaging capability not available in fluorescence microscopy, the dye molecules were found located within the shell and polymer-salt regions of the capsules (“1” and “2,” respectively, in Figure 3c) and not in these off-centered, polymer-free cores (“3,” Figure 3c). Though the actual internal NAC structure unexpectedly differs from the presumed capsule structure (Figure 2), we make the assumption that the nondye-containing region does not affect the release of dye from the rest of the capsule.

Estimation of the shell thickness and the parameter “x_1” can be performed using optical images of the capsules, but the fluorescence contrast between regions 1 and 2 is too slight to resolve (Figures 3b, c). However, we addressed this problem by suspending the capsules in glycine-NaOH buffers of varying pH values and collecting their fluorescence images (Figure 4). We anticipated that some higher pH value would cause the polymer-salt aggregate inside the capsule (region 2) to disassemble completely (due to neutralization of the PAH), thereby revealing the location of the inner shell wall. We found a pH of ~9.6 to be most appropriate for disassembling region 2 and not region 1 (the shell).

The shell thickness was determined by collecting intensity line profiles across the fluorescence image of capsules dispersed in pH 9.6 and measuring the average distance between the intensity midpoints on both sides of the left-hand and right-hand peaks (Figure 5a). The shell thickness was thus measured for 75 capsules of various sizes, resulting in the interesting observation that larger NACs had thicker shells (Figure 5b). The thickness-capsule diameter correlation was a linear one, yielding a slope from which the value of x_1 was calculated. The values of the partition coefficients P_{12} and P_{2b} were also determined from the line profile analysis shown in Figure 5. Ratio P_{12} was estimated by taking the average of the intensity ratios between shell and the core for all 75 particles, yielding $P_{12} = 0.648$; the ratio between the initial shell and core concentrations σ was estimated as $\sigma \approx 1/P_{12}$. Ratio P_{2b} was estimated similarly from intensity ratios between shell and the bulk ($P_{2b} = 0.126$).

Finally, the mean particle size and distribution of the capsules were estimated. Measuring the capsule size from optical images (Figure 3) would yield incorrect, skewed values because capsules below ~0.5 μm cannot be resolved with optical microscopy. On the other hand, SEM images (Figure 6a) can clearly resolve capsules from tens of nanometer to microns covering the entire range of capsule sizes. The capsule diameter distribution determined from SEM images gave a mean size of 3.12 ± 0.42 μm (relative standard deviation, RSD = 0.42/3.12 = 13.5%) based on a lognormal distribution fit of the data (Figure 6b). There was, however, a concern about capsules contracting when dried for SEM imaging, as was observed for other NAC materials.[10] To address this issue, we measured the diameter distribution of “wet” capsules using a Coulter counter. The Coulter counter allows for size distribution measurements of capsules in their wet state and with high statistical count (~33,000 capsules). Although capsules below 2 μm could not be sized, a lognormal distribution reasonably fit the collected data (Figure 6b). The mean size was 3.8 ± 0.54 μm (RSD = 14.2%), suggesting that the capsule diameter shrunk by ~18% after drying. The similarity in size distribution shape and the closeness in relative standard deviations for the wet and dry capsules gave confidence that the mean capsule diameter of 3.8 ± 0.54 μm accurately describes the size distribution of the dye-containing NACs.

Comparing experimental dye-release kinetics with our mathematical model

To compare the experimental release kinetics with the predictions of our analytical model, a characteristic radius for

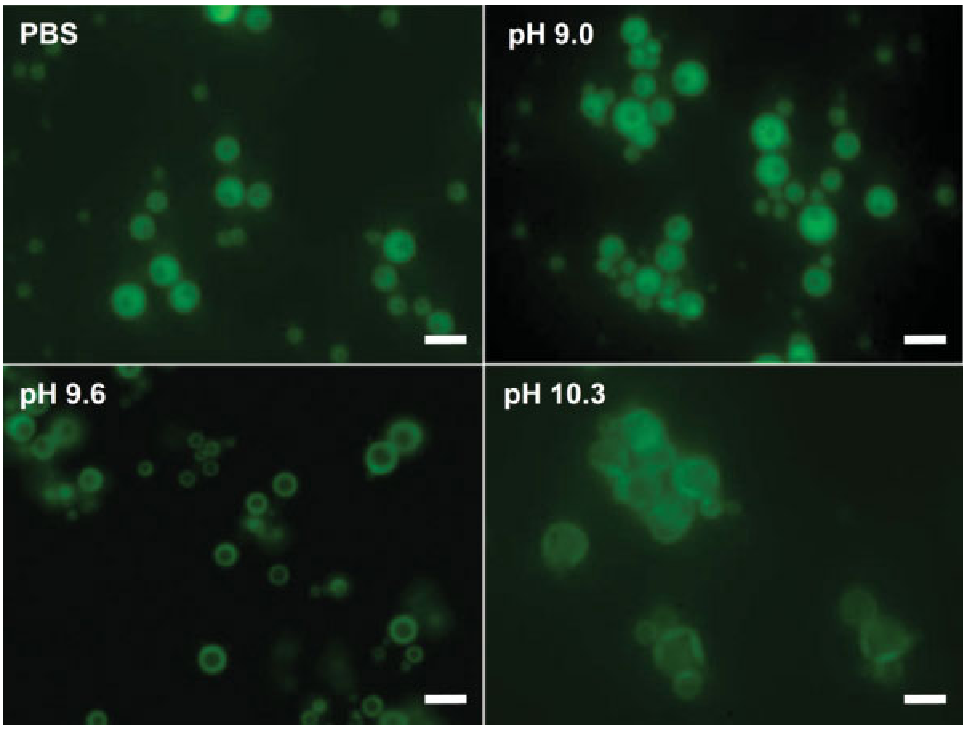

Figure 4. Fluorescence images of NACs dispersed in PBS and in glycine buffers of pH 9, 9.6, and 10.3, for shell thickness estimation purposes.

Scale bars: 10 μm. [Color figure can be viewed in the online issue, which is available at www.interscience.wiley.com.]

the microcapsules has to be defined. Our microcapsules were inherently polydisperse, with size distribution represented in Figure 6b. The particle size histogram in Figure 6b satisfies a lognormal distribution $g(R_2)$, with average size $\langle R_2 \rangle = 1.89$ μm and standard deviation $w = 0.54$ μm. Considering that the mass released by the diffusion mechanism is proportional to the external surface of the microcapsules, $4\pi R_2^2$, we weighted the size distribution by this factor to define the surface-weighted characteristic radius $\overline{R}_2$ for an equivalent monodisperse system

$$\overline{R}_2 = \frac{\int_{R_{2,\min}}^{R_{2,\max}} R_2^3 g(R_2) dR_2}{\int_{R_{2,\min}}^{R_{2,\max}} R_2^2 g(R_2) dR_2} \tag{23}$$

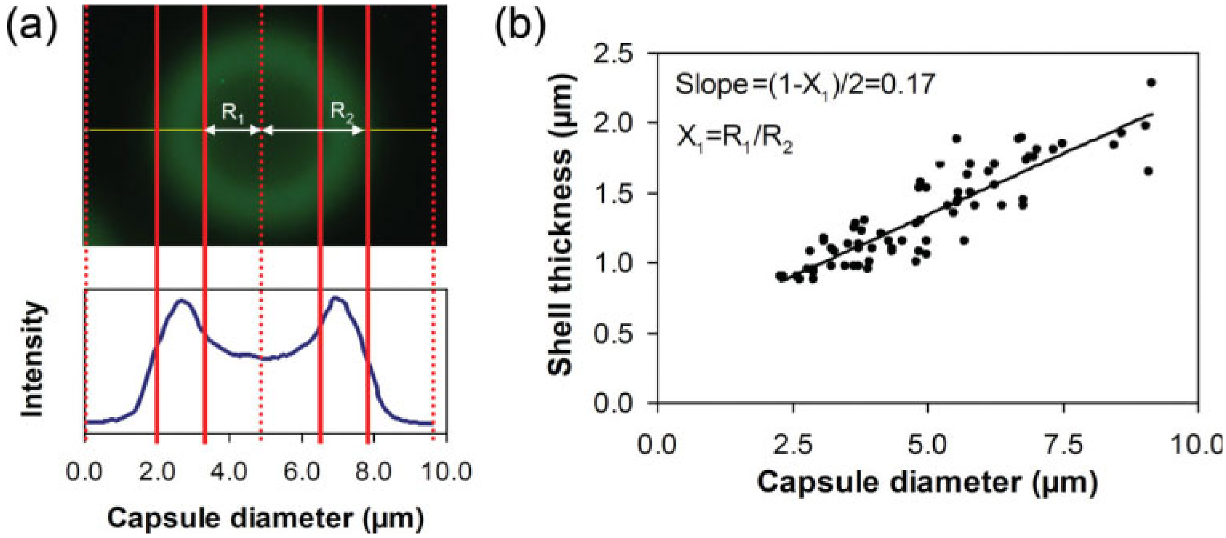

Figure 5. (a) Schematic of shell thickness analysis. (b) Correlation between particle size and shell thickness based on intensity line profiles of NACs at pH 9.6 (shown in Figure 4).

[Color figure can be viewed in the online issue, which is available at www.interscience.wiley.com.]

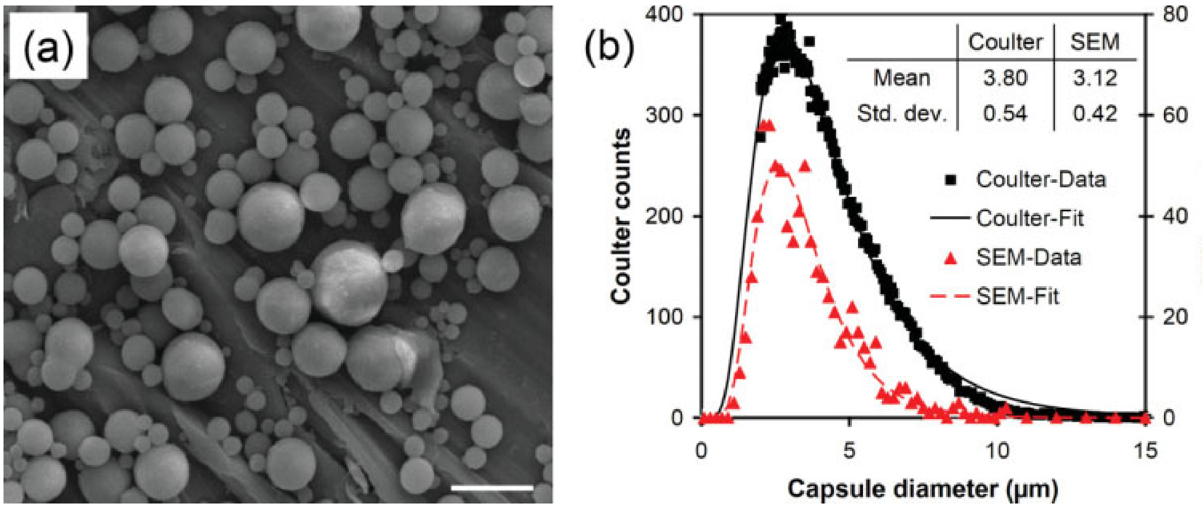

Figure 6. (a) Scanning electron microscope (SEM) image of NACs and (b) Capsule diameter distribution data from SEM images and Coulter counter measurements fitted to log-normal distribution.

[Color figure can be viewed in the online issue, which is available at www.interscience.wiley.com.]

In Figure 7, we present the experimental release kinetics from our capsules. In the same figure, we present the prediction of our theory after Eq. 21, for a system of monodisperse capsules with surface-weighted radius $\overline{R}_2 = 3.055$ μm calculated from Eq. 23.

A more rigorous, however mathematically more involved, way of taking into account polydispersity in our model is to average the release rate according to the formula

$$\left\langle \frac{M(t)}{M_\infty} \right\rangle = \frac{\int_{R_{2,\min}}^{R_{2,\max}} R_2^2 g(R_2) \frac{M(t,R_2)}{M_\infty} dR_2}{\int_{R_{2,\min}}^{R_{2,\max}} R_2^2 g(R_2) dR_2} \tag{24}$$

We notice that this definition, as expected, improves the agreement with the experimental data, as compared to the previous calculation considering an equivalent monodisperse system with surface-weighted radius $\overline{R}_2$, as defined in Eq. 23. Indeed, after taking into account polydispersity effects with Eq. 24, the model predictions are within error bars for the majority of data points.

Our model reproduces the asymptotic plateau in the release kinetics as observed in ours and also in other experimental systems previously reported in literature.[21,33,40,44,58,60–62,68] This important feature, which is captured by Eq. 21, is clearly a consequence of the gradual depletion of the microcapsule: As the amount of substance inside the capsule diminishes, as observed in the concentration profiles (Figure 8), the concentration gradient between the microcapsule and the external fluid diminishes, and so does the mass flux, according to Fick's law, until an equilibrium distribution governed by the partition coefficients of the solute between the shell and core, and the external fluid is achieved. This plateau effect cannot be reproduced by simplistic models such as the Higuchi equation,[63] which assumes a constant concentration gradient between the capsule and the external fluid (see Supporting Information for a discussion on the performance of this and other simplified models to fit our experimental data). Another salient feature of our model over previous analytical approaches for drug delivery is that it is able to capture the influence of the core-shell geometry of our spherical capsules in their transport properties. This is reflected in the dependence of the release kinetics on the value of $\gamma = D_2/D_1$, and on the shell thickness characterized by the parameter $x_1 = R_1/R_2$.

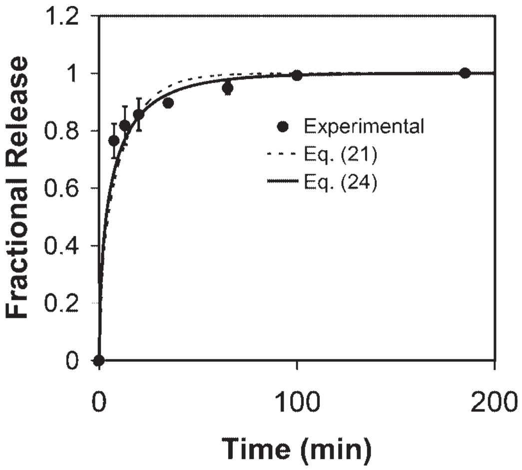

Figure 7. Experimental release profile, obtained as an average from three independent release studies, displayed with error bars.

Also shown is the prediction by our model Eq. 21, with parameters estimated from optical microscopy images: $x_1 = R_1/R_2 = 0.6506$, $P_{12} = 0.648$, $P_{2b} = 0.126$, $\sigma = 1.54$. The parameters fitted where $\gamma = D_2/D_1$, the core diffusion coefficient D_1, and the Bi number. The dashed line represents the model Eq. 21, evaluated at the surface-weighted radius $\overline{R}_2 = 3.055$ μm, for optimal fit values of $\gamma = 0.7$, $D_1 = 13 \times 10^{-16}$ (m^2/s), and $Bi = 1000$. Also shown, by the solid line, is the correction obtained by averaging the results of Eq. 21 over the different particle sizes, by employing the histogram in Figure 6b according to Eq. 24.

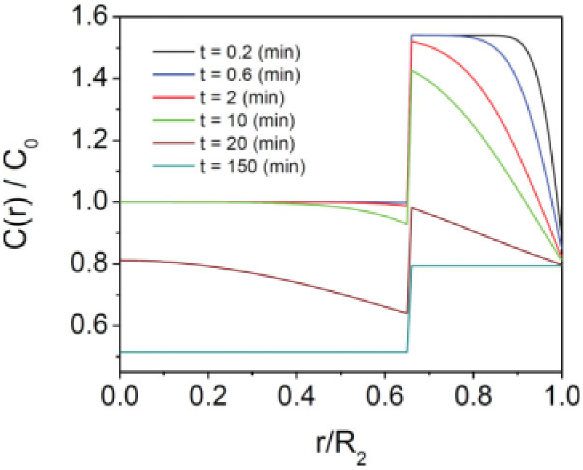

Figure 8. Normalized concentration profiles, at different times, predicted after Eq. 16.

The parameters estimated from experiments were used: $x_1 = R_1/R_2 = 0.6506$, $P_{12} = 0.648$, $P_{2b} = 0.126$, $\sigma = 1.54$. The surface-weighted radius $\bar{R}_2 = 3.055$ μm was calculated after Eq. 23. The values $\gamma = 0.7$, $D_1 = 13 \times 10^{-16}$ (m^2/s), and $Bi = 1000$, obtained from the release curve in Figure 7, were used. [Color figure can be viewed in the online issue, which is available at www.interscience.wiley.com.]

From the experimental fit, we were able to obtain experimental estimations for three physical parameters as free parameters through least-squares method fitting: the ratio between the outer shell and inner core effective diffusion coefficients $\gamma = D_2/D_1 = 0.7$, the effective diffusion coefficient for the core $D_1 = 13 \times 10^{-16}$ (m^2/s), and $Bi = 1000$. This procedure required evaluating the series Eq. 21 at each time, and iterate for the values of D_1, γ, and Bi which minimize the square of the error with respect to the experimental data points. In the evaluation of the series, we found that truncation up to 50 terms was enough to achieve convergence within machine precision 10^{-14}. The very large Bi number indicated that the experimental boundary layer mass transfer resistance was negligible. Indeed, in numerical evaluation of Eq. 21, for $Bi \approx 1000$ or larger the fractional release becomes independent of this parameter, and thus the results reduce to the case of negligible boundary layer resistance.

From these values, we estimated the effective diffusion coefficient in the shell as $D_2 = 9.1 \times 10^{-16}$ (m^2/s). These small values, which represent a phenomenological rather than a molecular property, are close in order-of-magnitude to that observed in experimental drug delivery systems for diffusion of fluorescein from other polyelectrolyte spherical capsular materials, 10^{-16} m^2/s.[107,108] Both core and shell diffusion coefficients were of the same order of magnitude, as expected on physical grounds from the experimental estimations for the partition coefficient between shell and core, $P_{12} = 0.648$.

Finally, to provide experimental validation of the diffusion coefficient of the core, we studied the diffusion of sodium fluorescein through polymer-salt matrix films through the QCM-D technique. This mass-based measurement approach allowed for highly sensitive quantification of dye adsorption by the films. Based on the dissipation values, the film could be assumed to be a rigid, nonviscoelastic film, allowing the Sauerbrey model to be properly applied for mass and thickness calculations[109] (manuscript in preparation). The calculated thickness of the deposited PAH/cit film was ~150 nm. By assuming one-dimensional molecular transport for Na–Flu through the film and using Fick's second law, we derived a diffusion coefficient of ~10^{-19} m^2/s, which was in good agreement with the measured diffusion of rhodamine dye in layer-by-layer-assembled polyelectrolyte films.[110]

Conclusions

Extending the general mathematical formalism introduced by Ramkrishna and Amundson,[88] an analytical solution to describe unsteady-state mass transport from spherical capsules comprised of multiple shells was derived, by accounting for the shells and core via effective diffusion coefficients. It successfully captured the asymptotic plateau effect of diffusive release, as verified by experimental data of dye release from single-shell nanoparticle/polymer capsules. Modeling further captured the observation that capsule dye concentration diminished with time but did not deplete completely, and the effects of capsule diameter and shell thickness distribution on dye release. Special sample preparation and characterization procedures were developed for analyzing suspension of micron-sized, dye-containing capsules via optical fluorescence microscopy. This resulted in new structural information about the nanoparticle-assembled capsules, such as the presence of a polymer-free region within the polymer/salt network in the capsule interior, and the linear dependence of shell thickness on capsule diameter. The analytical model allowed for diffusion coefficients in the capsule shell and core to be estimated, which were found comparable to experimental values for the similar systems reported in the literature. The modeling approach presented here can be extended as a useful tool for analyzing multi-layered capsular materials and chemical reaction-transport scenarios.

Acknowledgments

This work was supported by a training fellowship from the Nanobiology Training Program from the W. M. Keck Center for Interdisciplinary Bioscience Training of the Gulf Coast Consortia (NIH Grant No. 1 T90 DK70121-01 and R90 DK71504-01), the National Science Foundation (CBET-0652073), a 3M Non-tenured Faculty Award, and a Rice University Institute of Biosciences and Bioengineering Medical Innovations Grant. We thank Dr. Qilin Li for allowing us to use QCM-D and Dr. Archana Jaiswal (Q-sense) for helpful discussions in QCM-D analysis. The authors acknowledge Prof. Michael W. Deem and Gautam C. Kini for helpful discussions.

Notation

B_1, B_2 = coefficients in the eigenfunctions expansion, Eq. 10.
$c(x)$ = coefficient for the general Sturm–Liouville problem, Eq. A4.
$C(r,t)$ = concentration profile inside the microcapsule.
C_0 = initial concentration in the core region of the microcapsule.
C_b = concentration in the external bulk fluid surrounding the microcapsule.
C_s = concentration in the external surface of the microcapsule.

D_1 = effective diffusion coefficient in the inner core.

D_2 = effective diffusion coefficient in the outer shell.

Đ(x) = dimensionless diffusion coefficient as a function of the dimensionless radial distance inside the microcapsule, defined by Eq. A10.

$\hat{L}$ = Sturm–Liouville differential operator.

$L_2[0,1]$ = space of Lebesgue-square integrable functions in the interval $x \in [0,1]$.

M_{12}, M_{21}, M_{22} = matrix elements in the eigenvalue problem, Eq. A22.

P_{12} = partition coefficient for the diffusing substance between the core and shell.

P_{n} = positive coefficients in the inner product Eq. A2.

$p(x)$ = coefficient in the general Sturm–Liouville operator, Eq. A1.

r = radial coordinate inside the microcapsule.

R_1 = radius of the core.

R_2 = external radius of the microcapsule.

t = time

$v_k\,(x)$ = eigenfunction for the Sturm–Liouville problem, Eq. 13.

$x \equiv r/R_2$ = dimensionless radial distance.

$x_1 \equiv R_1/R_2$ = ratio between the inner core and external radii of the microcapsule.

Greek letters

$\Phi(x, \tau) \equiv (C(r, t) - C_{\mathrm{b}})/C_0$ = dimensionless concentration.

α_k = dimensionless coefficients, defined in Eq. 14.

$\gamma \equiv D_2/D_1$ = ratio between the effective diffusion coefficients of the external shell and inner core of the microcapsule.

λ_k = eigenvalues of a Sturm–Liouville problem.

$\tau \equiv tD_1/R_2^2$ = dimensionless time.

σ = ratio between the shell and core initial concentrations.

Literature Cited

1. Gregoriades G, editor. *Liposomal Technology*, 2nd ed. Boca Raton, FL: CRC Press, 1993:1–3.
2. Lasic D. Liposomes. *Am Sci*. 1992;80:20–31.
3. Torchilin VP, Trubetskoy VS, Milshteyn AM, Canillo J, Wolf GL, Papisov MI, Bogdanov AA, Narula J, Khaw BA, Omelyanenko VG. Targeted delivery of diagnostic agents by surface-modified liposomes. *J Control Release*. 1994;28:45–58.
4. Srivastava A, Eisenthal KB. Kinetics of molecular transport across a liposome bilayer. *Chem Phys Lett*. 1998;292:345–351.
5. Ross PC, Hensen ML, Supabphol R, Hui SW. Multilamellar cationic liposomes are efficient vectors for in vitro gene transfer in serum. *J Liposome Res*. 1998;8:499–520.
6. Skirtach AG, Dejugnat C, Braun D, Susha AS, Rogach AL, Parak WJ, Mohwald H, Sukhorukov GB. The role of metal nanoparticles in remote release of encapsulated materials. *Nano Lett*. 2005;5:1371–1377.
7. Caruso F, Caruso RA, Mohwald H. Nanoengineering of inorganic and hybrid hollow spheres by colloidal templating. *Science*. 1998;282:1111–1114.
8. Skirtach AG, Javier AM, Kreft O, Kohler K, Alberola AP, Mohwald H, Parak WJ, Sukhorukov GB. Laser-induced release of encapsulated materials inside living cells. *Angew Chem Int Ed*. 2006;45:4612–4617.
9. Yu J, Murthy VS, Rana RK, Wong MS. Synthesis of nanoparticle-assembled tin oxide/polymer microcapsules. *Chem Commun*. 2006:1097–1099.
10. Rana RK, Murthy VS, Yu J, Wong MS. Nanoparticle self-assembly of hierarchically ordered microcapsule structures. *Adv Mater*. 2005;17:1145–1150.
11. Murthy VS, Rana RK, Wong MS. Nanoparticle-assembled capsule synthesis: formation of colloidal polyamine-salt intermediates. *J Phys Chem B*. 2006;110:25619–25627.
12. Kadali SB, Soultanidis N, Wong MS. Assembling colloidal silica into porous hollow microspheres. *Top Catal*. 2008;49:251–258.
13. Fischer S, Foerg C, Ellenberger S, Merkle HP, Gander B. One-step preparation of polyelectrolyte-coated PLGA microparticles and their functionalization with model ligands. *J Control Release*. 2006;111:135–144.
14. Chen HM, Wei OY, Jones M, Metz T, Martoni C, Haque T, Cohen R, Lawuyi B, Prakash S. Preparation and characterization of novel polymeric microcapsules for live cell encapsulation and therapy. *Cell Biochem Biophys*. 2007;47:159–167.
15. Schlocker W, Gschliesser S, Bernkop-Schnurch A. Evaluation of the potential of air jet milling of solid protein-poly(acrylate) complexes for microparticle preparation. *Eur J Pharm Biopharm*. 2006;62:260–266.
16. Lameiro MH, Lopes A, Martins LO, Alves PM, Melo E. Incorporation of a model protein into chitosan-bile salt microparticles. *Int J Pharm*. 2006;312:119–130.
17. Iemma F, Spizzirri UG, Puoci F, Muzzalupo R, Trombino S, Cassano R, Leta S, Picci N. pH-Sensitive hydrogels based on bovine serum albumin for oral drug delivery. *Int J Pharm*. 2006;312:151–157.
18. Dai CY, Wang BC, Zhao HW, Li B, Wang H. Preparation and characterization of liposomes-in-alginate (LIA) for protein delivery system. *Colloids Surf B Biointerfaces*. 2006;47:205–210.
19. Quaglia F, Ostacolo L, Nese G, De Rosa G, La Rotonda MI, Palumbo R, Maglio G. Microspheres made of poly(epsilon-caprolactone)-based amphiphilic copolymers: potential in sustained delivery of proteins. *Macromol Biosci*. 2005;5:945–954.
20. Zhang Y, Zhu W, Ding JD. Preparation of thermosensitive microgels via suspension polymerization using different temperature protocols. *J Biomed Mater Res A*. 2005;75A:342–349.
21. Wang SB, Xu FH, He HS, Weng LJ. Novel alginate-poly(L-histidine) microcapsules as drug carriers: in vitro protein release and short term stability. *Macromol Biosci*. 2005;5:408–414.
22. Liu JB, Zeng FQ, Allen C. Influence of serum protein on polycarbonate-based copolymer micelles as a delivery system for a hydrophobic anti-cancer agent. *J Control Release*. 2005;103:481–497.
23. Cruz L, Schaffazick SR, Dalla Costa T, Soares LU, Mezzalira G, da Silveira NP, Schapoval EES, Pohlmann AR, Guterres SS. Physico-chemical characterization and in vivo evaluation of indomethacin ethyl ester-loaded nanocapsules by PCS, TEM, SAXS, interfacial alkaline hydrolysis and antiedematogenic activity. *J Nanosci Nanotechnol*. 2006;6:3154–3162.
24. Devarajan PV, Sonavane GS. Preparation and in vitro/in vivo evaluation of gliclazide loaded Eudragit nanoparticles as a sustained release carriers. *Drug Dev Ind Pharm*. 2007;33:101–111.
25. Chan Y, Bulmus V, Zareie MH, Byrne FL, Barner L, Kavallaris M. Acid-cleavable polymeric core-shell particles for delivery of hydrophobic drugs. *J Control Release*. 2006;115:197–207.
26. Mainardes RM, Chaud MV, Gremiao MPD, Evangelista RC. Development of praziquantel-loaded PLGA nanoparticles and evaluation of intestinal permeation by the everted gut Sac model. *J Nanosci Nanotechnol*. 2006;6:3057–3061.
27. Obeidat WM, Price JC. Preparation and evaluation of Eudragit S 100 microspheres as pH-sensitive release preparations for piroxicam and theophylline using the emulsion-solvent evaporation method. *J Microencapsul*. 2006;23:195–202.
28. Jaspart S, Bertholet P, Piel G, Dogne JM, Delattre L, Evrard B. Solid lipid microparticles as a sustained release system for pulmonary drug delivery. *Eur J Pharm Biopharm*. 2007;65:47–56.
29. Wang LQ, Cui FD. Chitosan-thioglycolic acid conjugate microspheres: their use for oral delivery of rEPO. *J Drug Deliv Sci Technol*. 2006;16:421–426.
30. Wang YS, Liu LR, Jiang Q, Zhang QQ. Self-aggregated nanoparticles of cholesterol-modified chitosan conjugate as a novel carrier of epirubicin. *Eur Polym J*. 2007;43:43–51.

31. Lin YH, Mi FL, Chen CT, Chang WC, Peng SF, Liang HF, Sung HW. Preparation and characterization of nanoparticles shelled with chitosan for oral insulin delivery. *Biomacromolecules*. 2007; 8:146–152.
32. Zhang WF, Chen XG, Li PW, He QZ, Zhou HY. Chitosan and chitosan/beta-cyclodextrin microspheres as sustained-release drug carriers. *J Appl Polym Sci*. 2007;103:1183–1190.
33. Zhou HY, Chen XG, Liu CS, Meng XH, Yu LJ, Liu XY, Liu N. Chitosan/cellulose acetate microspheres preparation and ranitidine release in vitro. *Pharm Dev Technol*. 2005;10:219–225.
34. Ko JA, Park HJ, Hwang SJ, Park JB, Lee JS. Preparation and characterization of chitosan microparticles intended for controlled drug delivery. *Int J Pharm*. 2002;249:165–174.
35. Sezer AD, Akbuga J. Fucosphere—new microsphere carriers for peptide and protein delivery: preparation and in vitro characterization. *J Microencapsul*. 2006;23:513–522.
36. Wang CQ, Li GT, Tao SY, Guo RR, Yan Z. Crystalline and micellar properties of amphiphilic biodegradable chitooligosaccharide-graft-poly(epsilon-caprolactone) copolymers. *Carbohydr Polym*. 2006;64:466–472.
37. Parodi B, Sillo G, Russo E, Caviglioli G, Cafaggi S, Bignardi G. Optimization of cross-linked high amylose starch microspheres containing 5-fluorouracil. *J Drug Deliv Sci Technol*. 2006;16:427–435.
38. Martinez-Sancho C, Herrero-Vanrell R, Negro S. Vitamin A palmitate and aciclovir biodegradable microspheres for intraocular sustained release. *Int J Pharm*. 2006;326:100–106.
39. Chen LY, Subirade M. Alginate-whey protein granular microspheres as oral delivery vehicles for bioactive compounds. *Biomaterials*. 2006;27:4646–4654.
40. Liu SQ, Tong YW, Yang YY. Incorporation and in vitro release of doxorubicin in thermally sensitive micelles made from poly(*N*-isopropylacrylamide-co-*N*,*N*-dimethylacrylamide)-b-poly(D,L-lactide-co-glycolide) with varying compositions. *Biomaterials*. 2005;26: 5064–5074.
41. Tian L, Hammond PT. Comb-dendritic block copolymers as tree-shaped macromolecular amphiphiles for nanoparticle self-assembly. *Chem Mater*. 2006;18:3976–3984.
42. Giacomelli C, Le Men L, Borsali R, Lai-Kee-Him J, Brisson A, Armes SP, Lewis AL. Phosphorylcholine-based pH-responsive diblock copolymer micelles as drug delivery vehicles: light scattering, electron microscopy, and fluorescence experiments. *Biomacromolecules*. 2006;7:817–828.
43. Crothers M, Zhou ZY, Ricardo NMPS, Yang Z, Taboada P, Chaibundit C, Attwood D, Booth C. Solubilisation in aqueous micellar solutions of block copoly(oxyalkylene)s. *Int J Pharm*. 2005; 293:91–100.
44. Zhang Y, Zhuo RX. Synthesis and drug release behavior of poly (trimethylene carbonate)-poly(ethylene glycol)-poly(trimethylene carbonate) nanoparticles. *Biomaterials*. 2005;26:2089–2094.
45. Oh KT, Bronich TK, Kabanov AV. Micellar formulations for drug delivery based on mixtures of hydrophobic and hydrophilic Pluronic((R)) block copolymers. *J Control Release*. 2004;94:411–422.
46. Tang YQ, Liu SY, Armes SP, Billingham NC. Solubilization and controlled release of a hydrophobic drug using novel micelle-forming ABC triblock copolymers. *Biomacromolecules*. 2003;4: 1636–1645.
47. Ge HX, Hu Y, Jiang XQ, Cheng DM, Yuan YY, Bi H, Yang CZ. Preparation, characterization, and drug release behaviors of drug nimodipine-loaded poly(epsilon-caprolactone)-poly(ethylene oxide)-poly(epsilon-caprolactone) amphiphilic triblock copolymer micelles. *J Pharm Sci*. 2002;91:1463–1473.
48. Hagan SA, Coombes AGA, Garnett MC, Dunn SE, Davis MC, Illum L, Davis SS, Harding SE, Purkiss S, Gellert PR. Polylactide-poly(ethylene glycol) copolymers as drug delivery systems. I. Characterization of water dispersible micelle-forming systems. *Langmuir*. 1996;12:2153–2161.
49. Zawaneh PN, Doody AM, Zelikin AN, Putnam D. Diblock copolymers based on dihydroxyacetone and ethylene glycol: synthesis, characterization, and nanoparticle formulation. *Biomacromolecules*. 2006;7:3245–3251.
50. Huang JJ, Wigent RJ, Schwartz JB. Nifedipine molecular dispersion in microparticles of ammonio methacrylate copolymer and ethylcellulose binary blends for controlled drug delivery: effect of matrix composition. *Drug Dev Ind Pharm*. 2006;32:1185–1197.
51. Oh KT, Bronich TK, Bromberg L, Hatton TA, Kabanov AV. Block ionomer complexes as prospective nanocontainers for drug delivery. *J Control Release*. 2006;115:9–17.
52. Gao CS, Huang J, Jiao Y, Shan L, Liu Y, Li Y, Mei XG. In vitro release and in vivo absorption in beagle dogs of meloxicam from Eudragit (R) FS 30 D-coated pellets. *Int J Pharm*. 2006;322:104–112.
53. Gaber NN, Darwis Y, Peh KK, Tan YTF. Characterization of polymeric micelles for pulmonary delivery of beclomethasone dipropionate. *J Nanosci Nanotechnol*. 2006;6:3095–3101.
54. Wei H, Zhang XZ, Zhou Y, Cheng SX, Zhuo RX. Self-assembled thermoresponsive micelles of poly(*N*-isopropylacrylamide-b-methyl methacrylate). *Biomaterials*. 2006;27:2028–2034.
55. Liu XM, Yang YY, Leong KW. Thermally responsive polymeric micellar nanoparticles self-assembled from cholesteryl end-capped random poly(*N*-isopropylacrylamide-co-*N*,*N*-dimethylacrylamide): synthesis, temperature-sensitivity, and morphologies. *J Colloid Interface Sci*. 2003;266:295–303.
56. Kurkuri MD, Aminabhavi TM. Poly(vinyl alcohol) and poly(acrylic acid) sequential interpenetrating network pH-sensitive microspheres for the delivery of diclofenac sodium to the intestine. *J Control Release*. 2004;96:9–20.
57. Gupta KC, Kumar MNVR. Preparation, characterization and release profiles of pH-sensitive chitosan beads. *Polym Int*. 2000;49:141–146.
58. Kayaman-Apohan N, Akdemir ZS. Synthesis and characterization of pendant carboxylic acid functional poly(lactic acid) and poly (lactic acid-co-glycolic acid) and their drug release behaviors. *Polym Adv Technol*. 2005;16:807–812.
59. Zaghloul AAA, Mustafa F, Siddiqu A, Khan M. Biodegradable microparticulates of beta-estradiol: preparation and in vitro characterization. *Drug Dev Ind Pharm*. 2005;31:803–811.
60. Desai KGH, Park HJ. Preparation and characterization of drug-loaded chitosan-tripolyphosphate microspheres by spray drying. *Drug Dev Res*. 2005;64:114–128.
61. Liu MX, Dong J, Yang YJ, Yang XL, Xu HB. Characterization and release of triptolide-loaded poly (D,L-lactic acid) nanoparticles. *Eur Polym J*. 2005;41:375–382.
62. Miyazaki Y, Yakou S, Nagai T, Takayama K. Release profiles of theophylline from microspheres consisting of dextran derivatives and cellulose acetate butyrate: effect of polyion complex formation. *Drug Dev Ind Pharm*. 2003;29:795–804.
63. Higuchi T. Rate of release of medicaments from ointment bases containing drugs in suspension. *J Pharm Sci*. 1961;50:874–875.
64. Higuchi T. Mechanism of sustained-action medication—theoretical analysis of rate of release of solid drugs dispersed in solid matrices. *J Pharm Sci*. 1963;52:1145–1149.
65. Faisant N, Akiki J, Siepmann F, Benoit JP, Siepmann J. Effects of the type of release medium on drug release from PLIGA-based microparticles: experiment and theory. *Int J Pharm*. 2006;314: 189–197.
66. Liu CS, Desai KGH, Tang XX, Chen XG. Drug release kinetics of spray-dried chitosan microspheres. *Dry Technol*. 2006;24:769–776.
67. Kanjickal DG, Lopina ST. Modeling of drug release from polymeric delivery systems—a review. *Crit Rev Ther Drug Carrier Syst*. 2004;21:345–386.
68. Faisant N, Siepmann J, Richard J, Benoit JP. Mathematical modeling of drug release from bioerodible microparticles: effect of gamma-irradiation. *Eur J Pharm Biopharm*. 2003;56:271–279.
69. Siepmann J, Gopferich A. Mathematical modeling of bioerodible, polymeric drug delivery systems. *Adv Drug Del Rev*. 2001;48: 229–247.
70. Jo YS, Kim MC, Kim DK, Kim CJ, Jeong YK, Kim KJ, Muhammed M. Mathematical modelling on the controlled-release of indomethacin-encapsulated poly(lactic acid-co-ethylene oxide) nanospheres. *Nanotechnology*. 2004;15:1186–1194.
71. Frenning G. Theoretical investigation of drug release from planar matrix systems: effects of a finite dissolution rate. *J Control Release*. 2003;92:331–339.
72. Abdekhodaie MJ. Diffusional release of a solute from a spherical reservoir into a finite external volume. *J Pharm Sci*. 2002;91: 1803–1809.
73. Polakovic M, Gorner T, Gref R, Dellacherie E. Lidocaine loaded biodegradable nanospheres. II. Modelling of drug release. *J Control Release*. 1999;60:169–177.

74. Vanbommel EMG, Dezentje RFR, Crommelin DJA, Fokkens JG. Drug release kinetics from the gradient matrix system—mathematical-modeling. *Int J Pharm*. 1991;72:19–27.
75. Faisant N, Siepmann J, Benoit JP. PLGA-based microparticles: elucidation of mechanisms and a new, simple mathematical model quantifying drug release. *Eur J Pharm Sci*. 2002;15:355–366.
76. Siepmann J, Peppas NA. Mathematical modeling of controlled drug delivery. *Adv Drug Del Rev*. 2001;48:137–138.
77. Kosmidis K, Argyrakis P, Macheras P. A reappraisal of drug release laws using Monte Carlo simulations: the prevalence of the Weibull function. *Pharm Res*. 2003;20:988–995.
78. Li H, Yan GP, Wu SN, Wang ZJ, Lam KY. Numerical simulation of controlled nifedipine release from chitosan microgels. *J Appl Polym Sci*. 2004;93:1928–1937.
79. Siepmann J, Faisant N, Benoit JP. A new mathematical model quantifying drug release from bioeridible microparticles using Monte Carlo simulations. *Pharm Res*. 2002;19:1885–1893.
80. Siepmann J, Peppas NA. Hydrophilic matrices for controlled drug delivery: an improved mathematical model to predict the resulting drug release kinetics (the 'sequential' layer model). *Pharm Res*. 2000;17:1290–1298.
81. Siepmann J, Streubel A, Peppas NA. Understanding and predicting drug delivery from hydrophilic matrix tablets using the "sequential layer" model. *Pharm Res*. 2002;19:306–314.
82. Frenning G, Stromme M. Drug release modeled by dissolution, diffusion, and immobilization. *Int J Pharm*. 2003;250:137–145.
83. Siepmann J, Podual K, Sriwongjanya M, Peppas NA, Bodmeier R. A new model describing the swelling and drug release kinetics from hydroxypropyl methylcellulose tablets. *J Pharm Sci*. 1999; 88:65–72.
84. Zygourakis K. Discrete simulations and bioerodible controlled release systems. *Polym Prep ACS 30*, 1989;456–457.
85. Zygourakis K. Development and temporal evolution of erosion fronts in bioerodible controlled release devices. *Chem Eng Sci*. 1990;45:2359–2366.
86. Gienger G, Knoch A, Merkle HP. Modeling and numerical computation of drug transport in laminates—model case evaluation of transdermal delivery system. *J Pharm Sci*. 1986;75:9–15.
87. Kalia YN, Guy RH. Modeling transdermal drug release. *Adv Drug Deliv Rev*. 2001;48:159–172.
88. Ramkrishna D, Amundson NR. Transport in composite-materials—reduction to a self-adjoint formalism. *Chem Eng Sci*. 1974;29:1457–1464.
89. Locke BR, Arce P, Park Y. Applications of self-adjoint operators to electrophoretic transport, enzyme-reactions, and microwave-heating problems in composite media. II. Electrophoretic transport in layered membranes. *Chem Eng Sci*. 1993;48:4007–4022.
90. Vaidya DS, Nitsche JM, Diamond SL, Kofke DA. Convection-diffusion of solutes in media with piecewise constant transport properties. *Chem Eng Sci*. 1996;51:5299–5312.
91. Locke BR, Arce P. Applications of self-adjoint operators to electrophoretic transport, enzyme-reactions, and microwave-heating problems in composite media. I. General formulation. *Chem Eng Sci*. 1993;48:1675–1686.
92. Lu XS, Viljanen M. An analytical method to solve heat conduction in layered spheres with time-dependent boundary conditions. *Phys Lett A*. 2006;351:274–282.
93. Fredman TP. An analytical solution method for composite layer diffusion problems with an application in metallurgy. *Heat Mass Transf*. 2003;39:285–295.
94. Johnston PR. Diffusion in composite media—solution with simple eigenvalues and eigenfunctions. *Math Comput Model*. 1991;15:115–123.
95. Bouzidi M. Transient heat diffusion in multilayered composite media and eigenvalue problem. I. A single multilayered wall. *Int J Heat Mass Transf*. 1991;34:1259–1270.
96. Mikhailov MD, Ozisik MN, Vulchanov NL. Diffusion in composite layers with automatic solution of the eigenvalue problem. *Int J Heat Mass Transf*. 1983;26:1131–1141.
97. Mitlin V, Bromberg L. Analysis of diffusion through composite membranes. I. Mathematical development. *Chem Eng Sci*. 1992; 47:695–703.
98. Dong W, Bodmeier R. Encapsulation of lipophilic drugs within enteric microparticles by a novel coacervation method. *Int J Pharm*. 2006;326:128–138.
99. Katsikogianni G, Avgoustakis K. Poly(lactide-co-glycolide)-methoxy-poly(ethylene glycol) nanoparticles: drug loading and release properties. *J Nanosci Nanotechnol*. 2006;6:3080–3086.
100. Formariz TR, Sarmento VHV, Silva-Junior AA, Scarpa MV, Santilli CV, Oliveira AG. Doxorubicin biocompatible O/W microemulsion stabilized by mixed surfactant containing soya phosphatidylcholine. *Colloids Surf B Biointerfaces*. 2006;51:54–61.
101. Memisoglu-Bilensoy E, Sen M, Hincal AA. Effect of drug physicochemical properties on in vitro characteristics of amphiphilic cyclodextrin nanospheres and nanocapsules. *J Microencapsul*. 2006;23:59–68.
102. Belfiore LA. Laminar boundary layer mass transfer around solid spheres, gas bubbles, and other submerged objects. In: *Transport Phenomena for Chemical Reactor Design*, 1st ed. Hoboken, New Jersey: John Wiley and Sons, 2002:275–360.
103. Morse PM, Feshbach H. Boundary conditions and eigenfunctions. In: *Methods of Theoretical Physics,* Vol. 1. New York: McGraw-Hill, 1953:676–790.
104. Carslaw HS, Jaeger JC. *Conduction of Heat in Solids*, 2nd ed., New York: Oxford University press, 1959.
105. Crank J. *The Mathematics of Diffusion*, 2nd ed. New York: Oxford University press, 1975.
106. Kärger J, Douglas MR. *Diffusion in Zeolites and Other Microporous Solids*, 1st ed. New York: John Wiley & Sons, 1992.
107. Peyratout CS, Dahne L. Tailor-made polyelectrolyte microcapsules: from multilayers to smart containers. *Angew Chem Int Ed*. 2004;43:3762–3783.
108. Antipov AA, Sukhorukov GB. Polyelectrolyte multilayer capsules as vehicles with tunable permeability. *Adv Colloid Interface Sci*. 2004;111:49–61.
109. Kotarek JA, Johnson KC, Moss MA. Quartz crystal microbalance analysis of growth kinetics for aggregation intermediates of the amyloid-beta protein. *Anal Biochem*. 2008;378:15–24.
110. VonKlitzing R, Mohwald H. A realistic diffusion model for ultrathin polyelectrolyte films. *Macromolecules*. 1996;29:6901–6906.

Appendix

As shown by Ramkrishna and Amundson,[88] most transport problems in one-dimensional, multilayered systems can be solved by obtaining the eigenvalues and eigenfunctions of a second-order Sturm–Liouville operator, generally defined by

$$\hat{L}u = -\frac{1}{\rho(x)}\frac{d}{dx}\left[p(x)\frac{d}{dx}u\right] + q(x)u \quad 0 < x < 1, \tag{A1}$$

and operating over functions $u(x)$ in a subspace of $L_2[0,1]$.

If the functions $\rho(x)$ and $p(x)$ are piecewise continuous, except in a countable, zero measure set of points $0 < x_1 < x_2 \dots < x_n < 1$, a generalized inner product can be defined[88] between functions u, v in the domain of $\hat{L}$

$$\langle u, v\rangle = \sum_{i=1}^{n+1} P_i \int\limits_{x_{i=1}}^{x_i} \rho(x)u(x)v(x)dx. \tag{A2}$$

Here, the P_i are strictly positive numbers, whose ratio $P_{i,i+1} = P_{i+1}/P_i$ defines the partitioning of solute between the different media separated by the interface located at x_i. The functions $u(x)$, $v(x)$ belong to a subspace of $L_2[0,1]$, where $\hat{L}$ is self-adjoint with respect to the inner product Eq. A2, i.e., $\langle \hat{L}u, v\rangle = \langle u, \hat{L}v\rangle$. Integration by parts allows one to readily show that

$$
\begin{aligned}
\langle \hat{L}u, v\rangle - \langle u, \hat{L}v\rangle &= P_{n+1}p(1)[u(1)v'(1) - u'(1)v(1)] \\
&\quad - P_1 p(0)[u(0)v'(0) - u'(0)v(0)] \\
&\quad + \sum_{i=1}^{n} \left[P_{i+1}p\left(x_i^+\right)\left[u\left(x_i^+\right)v'(x_i^+) - u'(x_i^+)v(x_i^+)\right]\right. \\
&\quad \left. - P_i p(x_i^-)\left[u\left(x_i^-\right)v'(x_i^-) - u'(x_i^-)v(x_i^-)\right]\right]
\end{aligned} \tag{A3}
$$

and the self-adjoint property of $\hat{L}$ is ensured provided that the boundary conditions on $u(x)$ and $v(x)$ are chosen such that the right-hand side of Eq. A3 vanishes.

In spherical and cylindrical geometries, when angular independence can be assumed, separation of variables or finite Fourier transform methods leads to the same general Sturm–Liouville form Eq. A1, where x represents a normalized radial coordinate and the functions $\rho(x)$ and $p(x)$ can be written in the general form

$$
\rho(x) = x^m c(x),\ p(x) = x^m\, k(x), \tag{A4}
$$

where $m = 1$ for cylinders, and $m = 2$ for spheres. In diffusion problems $c(x) = 1$, and $k(x)$ corresponds to a spatially distributed diffusion coefficient.

It is straightforward to show that, given the generalized expression for $p(x)$ in Eq. A4, a sufficient set of boundary conditions to be imposed on the functions $u(x)$, $v(x)$ for the right-hand side of Eq. A3 to vanish is given by

$$
\begin{aligned}
P_{n+1}p(1)[u(1)v'(1) - u'(1)v(1)] \\
- P_1 p(0)[u(0)v'(0) - u'(0)v(0)] = 0
\end{aligned} \tag{A5}
$$

$$
P_i u(x_i^+) = P_{i-1}u(x_i^-) \tag{A6}
$$

$$
k(x_i^+)\frac{du}{dx}(x_i^+) = k(x_i^-)\frac{du}{dx}(x_i^-). \tag{A7}
$$

This choice corresponds precisely with the physical conditions of partition of solute, as well as continuity of the mass flux at the interface between each pair of radial layers.

In particular, for the spherical shell geometry represented in Figure 2, the normalized radial coordinate is naturally defined by $x = r/R_2$, whereas the location of the interface is given by $x_1 = R_1/R_2$. Defining $P_{12} = P_2/P_1$ as the partition coefficient between both materials and choosing the value $P_1 = 1$ for the coefficient in the generalized inner product, Eq. A2 reduces to

$$
\langle u, v\rangle = \int_0^{x_1} x^2 u(x)v(x)dx + P_{12}\int_{x_1}^{1} x^2 u(x)v(x)dx \tag{A8}
$$

Solution method

In this section, we present in detail the mathematical analysis which provides the analytical equations presented in the main text.

For the mathematical treatment, it is convenient to define dimensionless variables, as follows

$$
x = r/R_2 \quad \tau = tD_1/R_2^2 \quad \gamma = D_2/D_1 \quad x_1 = R_1/R_2 \tag{A9}
$$

$$
\text{Đ}(x) = \begin{cases} 1 & 0 \le x < x_1 \\ \gamma & x_1 < x \le 1 \end{cases} \tag{A10}
$$

We also define a dimensionless concentration profile

$$
\Phi(x,\tau) = (C(r,t) - C^{\text{ss}}(r))/C_0 \tag{A11}
$$

Here, $C^{\text{ss}}(r)$ is the steady-state solution of Eq. 2, as defined in Eq. 7.

In dimensionless form, the differential Equation (2), with its initial, continuity and boundary conditions becomes

$$
\frac{1}{x^2}\frac{\partial}{\partial x}\left(x^2 \text{Đ}(x)\frac{\partial \Phi}{\partial x}\right) = \frac{\partial \Phi}{\partial \tau} \tag{A12}
$$

$$
\Phi(x,0) = \begin{cases} \left(C_0 - \frac{P_{12}}{P_{2\text{b}}}C_\text{b}\right)/C_0 & 0 \le x < x_1 \\ (\sigma C_0 - C_\text{b}/P_{2\text{b}})/C_0 & x_1 < x < 1 \end{cases} \tag{A13}
$$

$$
\frac{\partial \Phi}{\partial x}(1,\tau) = -Bi\,P_{2\text{b}}\,\Phi(1,\tau) \tag{A14}
$$

$$
\Phi\left(x_1^-,\tau\right) = P_{12}\Phi\left(x_1^+,\tau\right) \tag{A15}
$$

$$
\frac{\partial \Phi}{\partial x}\left(x_1^-,\tau\right) = \gamma\frac{\partial \Phi}{\partial x}\left(x_1^+,\tau\right) \tag{A16}
$$

$$
\lim_{x\to 0}\Phi(x,\tau) = \text{finite} \tag{A17}
$$

To solve the problem, we need to find the orthonormal set of eigenfunctions $v(x)$ and the corresponding eigenvalues λ of the self-adjoint differential operator $\hat{L}$, defined as

$$
\hat{L}v = -\frac{1}{x^2}\frac{d}{dx}\left(x^2 \text{Đ}\,(x)\frac{dv}{dx}\right) = \lambda v \tag{A18}
$$

The eigenfunctions must satisfy the continuity and boundary conditions

$$
\begin{aligned}
& v\left(x_1^-\right) = P_{12}v(x_1^+) \\
& \frac{dv}{dx}(x_1^-) = \gamma\frac{dv}{dx}(x_1^+) \\
& \frac{dv}{dx}(1) + Bi\,P_{2\text{b}}v(1) = 0 \\
& \lim_{x\to 0} v(x) = \text{finite}
\end{aligned} \tag{A19}
$$

The third boundary condition in Eq. A19, as well as the condition at the origin, are satisfied if the eigenfunctions are of the form

$$
v(x) = \begin{cases} B_1\frac{\sin(x\sqrt{\lambda})}{x} & 0 \le\ x < x_1 \\ B_2\left[\frac{\sin\left((1-x)\sqrt{\lambda/\gamma}\right)}{x} - \frac{\sqrt{\lambda/\gamma}}{1-P_{2\text{b}}Bi}\frac{\cos\left((1-x)\sqrt{\lambda/\gamma}\right)}{x}\right] & x_1 < x \le 1 \end{cases} \tag{A20}
$$

By applying the first two continuity conditions in Eq. A19 to the expression Eq. A20, we obtain a linear system for the coefficients B_1, B_2

$$
\begin{bmatrix} \sin(x_1\sqrt{\lambda}) & M_{12}(\lambda) \\ M_{21}(\lambda) & M_{22}(\lambda) \end{bmatrix}\begin{pmatrix} B_1 \\ B_2 \end{pmatrix} = \begin{pmatrix} 0 \\ 0 \end{pmatrix} \tag{A21}
$$

Here, the elements of the matrix are explicitly given by the formulas

$$\begin{aligned} M_{12}(\lambda) &= P_{12}\left[\frac{\sqrt{\lambda/\gamma}}{(1-P_{2\mathrm{b}}Bi)}\cos\Big((1-x_1)\sqrt{\lambda/\gamma}\Big) \right.\\ &\qquad \left. -\sin\Big((1-x_1)\sqrt{\lambda/\gamma}\Big)\right] \\ M_{21}(\lambda) &= \sqrt{\lambda}x_1\cos\Big(x_1\sqrt{\lambda}\Big)-\sin\Big(x_1\sqrt{\lambda}\Big) \\ M_{22}(\lambda) &= \gamma\left\{\sqrt{\frac{\lambda}{\gamma}}x_1\cos\Big((1-x_1)\sqrt{\lambda/\gamma}\Big)\right. \\ &\qquad +\sin\Big((1-x_1)\sqrt{\lambda/\gamma}\Big) \\ &\qquad +\frac{\sqrt{\lambda/\gamma}}{1-P_{2\mathrm{b}}Bi}\left\{\sqrt{\frac{\lambda}{\gamma}}x_1\sin\Big((1-x_1)\sqrt{\lambda/\gamma}\Big)\right. \\ &\qquad \left.\left. -\cos\Big((1-x_1)\sqrt{\lambda/\gamma}\Big)\right\}\right\} \end{aligned} \tag{A22}$$

For the linear system Eq. A21 to have nontrivial solutions, the determinant of the matrix in Eq. A21 must vanish. This condition provides a characteristic equation to obtain the (infinitely many) eigenvalues λ_k, $k = 1,2, \ldots, \infty$

$$\sin\Big(x_1\sqrt{\lambda}\Big) = \frac{M_{12}(\lambda)M_{21}(\lambda)}{M_{22}(\lambda)} \tag{A23}$$

From the linear system Eq. A21, we find $B_2(\lambda_k) = \alpha_k B_1(\lambda_k)$, and substituting into Eq. A20, we obtain the final expression for the eigenfunctions

$$v_k(x) = B_1(\lambda_k) \times \begin{cases} \frac{\sin(x\sqrt{\lambda_k})}{x} & 0 \le x < x_1 \\ \alpha_k\left[\frac{\sin\left((1-x)\sqrt{\lambda_k/\gamma}\right)}{x} - \frac{\sqrt{\lambda_k/\gamma}}{1-P_{2\mathrm{b}}Bi}\frac{\cos\left((1-x)\sqrt{\lambda_k/\gamma}\right)}{x}\right] & x_1 < x \le 1 \end{cases} \tag{A24}$$

Here, the constants α_k are defined by

$$\alpha_k = \frac{\sin\left(x_1\sqrt{\lambda_k}\right)}{P_{12}\left[\sin\Big((1-x_1)\sqrt{\lambda_k/\gamma}\Big) - \frac{\sqrt{\lambda_k/\gamma}}{1-P_{2\mathrm{b}}Bi}\cos\Big((1-x_1)\sqrt{\lambda_k/\gamma}\Big)\right]} \tag{A25}$$

The value of the coefficient $B_1(\lambda_k)$ is obtained by imposing the normalization condition over the eigenfunctions, $\langle v_k, v_k\rangle = 1$, to obtain

$$\begin{aligned} B_1(\lambda_k) = \Bigg[&\frac{1}{2}\left(x_1 - \frac{\sin\left(2x_1\sqrt{\lambda_k}\right)}{2\sqrt{\lambda_k}}\right) \\ &+ \alpha_k^2 P_{12}\left\{\frac{1}{2}\left(1 - x_1 - \frac{\sin\Big(2x_1\sqrt{\lambda_k/\gamma}\Big)}{2\sqrt{\lambda_k/\gamma}}\right)\right. \\ &+\frac{\cos\Big(2\sqrt{\lambda_k/\gamma}(1-x_1)\Big)-1}{2(1-P_{2\mathrm{b}}Bi)} \\ &\left.+\frac{\lambda_k/\gamma}{(1-P_{2\mathrm{b}}Bi)^2}\frac{1}{2}\left(1-x_1+\frac{\sin\Big(2x_1\sqrt{\lambda_k/\gamma}\Big)}{2\sqrt{\lambda_k/\gamma}}\right)\right\}\Bigg]^{-1/2} \end{aligned} \tag{A26}$$

To express the solution, subject to the initial condition Eq. A13, we use the finite Fourier transform method. For this purpose, we write Eq. A12 as

$$\frac{\partial\Phi}{\partial\tau} = -\hat{L}\Phi \tag{A27}$$

Let us calculate the inner product of Eq. A27 with an eigenfunction $v_k\,(x)$ of $\hat{L}$,

$$\frac{d}{d\tau}\langle v_k, \Phi\rangle = -\left\langle v_k, \hat{L}\Phi\right\rangle = -\left\langle \hat{L}v_k, \Phi\right\rangle \tag{A28}$$

Here, the self-adjoint property of $\hat{L}$ has been used. After Eq. A28, we obtain

$$\frac{d}{d\tau}\langle v_k, \Phi\rangle = -\lambda_k\langle v_k, \Phi\rangle \tag{A29}$$

Equation A29 is a first order differential equation for the time-dependent coefficient $\langle v_k, \Phi\rangle$, whose elementary solution is given by

$$\langle v_k, \Phi\rangle = \langle v_k, \Phi\rangle_0 e^{-\lambda_k\tau} \tag{A30}$$

The initial value $\langle v_k, \Phi\rangle_0$ is obtained from the initial condition Eq. A13, $\langle v_k, \Phi\rangle_0 = \langle v_k, \Phi(\tau = 0)\rangle$. We obtain the analytical expression

$$\begin{aligned} \langle v_k, \Phi\rangle_0 = B_1(\lambda_k)\Bigg[&\left(1-\frac{P_{12}}{P_{2\mathrm{b}}}\frac{C_\mathrm{b}}{C_0}\right)\left(\frac{\sin\left(x_1\sqrt{\lambda_k}\right)}{\lambda_k} - \frac{x_1\cos\left(x_1\sqrt{\lambda_k}\right)}{\sqrt{\lambda_k}}\right) \\ &+\left(\sigma - \frac{1}{P_{2\mathrm{b}}}\frac{C_\mathrm{b}}{C_0}\right)P_{12}\alpha_k\left(\frac{1-x_1\cos\Big((1-x_1)\sqrt{\lambda_k/\gamma}\Big)}{\sqrt{\lambda_k/\gamma}} - \frac{\sin\Big((1-x_1)\sqrt{\lambda_k/\gamma}\Big)}{\lambda_k/\gamma}\right. \\ &\left. - \frac{\sqrt{\lambda_k/\gamma}}{1-P_{2\mathrm{b}}Bi}\left(\frac{1-\cos\Big((1-x_1)\sqrt{\lambda_k/\gamma}\Big)}{\lambda_k/\gamma} + \frac{x_1\sin\Big((1-x_1)\sqrt{\lambda_k/\gamma}\Big)}{\sqrt{\lambda_k/\gamma}}\right)\right)\Bigg] \end{aligned} \tag{A31}$$

The final solution is therefore given by the series

$$
\begin{aligned}
\Phi(x,\tau) = \sum_{k=1}^{\infty} B_1(\lambda_k)\Bigg[&\left(1-\frac{P_{12}}{P_{2\mathrm{b}}}\frac{C_\mathrm{b}}{\mathrm{C}_0}\right)\left(\frac{\sin\left(x_1\sqrt{\lambda_k}\right)}{\lambda_k}-\frac{x_1\cos\left(x_1\sqrt{\lambda_k}\right)}{\sqrt{\lambda_k}}\right)\\
&+\left(\sigma-\frac{1}{P_{2\mathrm{b}}}\frac{C_\mathrm{b}}{\mathrm{C}_0}\right)P_{12}\alpha_k\left(\frac{1-x_1\cos\left((1-x_1)\sqrt{\lambda_k/\gamma}\right)}{\sqrt{\lambda_k/\gamma}}-\frac{\sin\left((1-x_1)\sqrt{\lambda_k/\gamma}\right)}{\lambda_k/\gamma}\right.\\
&\left.-\frac{\sqrt{\lambda_k/\gamma}}{1-P_{2\mathrm{b}}Bi}\left(\frac{1-\cos\left((1-x_1)\sqrt{\lambda_k/\gamma}\right)}{\lambda_k/\gamma}-\frac{x_1\sin\left((1-x_1)\sqrt{\lambda_k/\gamma}\right)}{\sqrt{\lambda_k/\gamma}}\right)\right)\Bigg]e^{-\lambda_k\tau}v_k(x) \qquad \text{(A32)}
\end{aligned}
$$

Manuscript received Jun. 27, 2008, revision received Nov. 21, 2008, and final revision received Mar. 19, 2009.